The Aeronautical Journal (2024), 1–25
doi:10.1017/aer.2024.121

ROYAL AERONAUTICAL SOCIETY

RESEARCH ARTICLE

Study of performance of an internal strut-based thrust vectoring control system

Harish Soundararajan[1,2] and B.T.N. Sridhar[1]

[1]Department of Aerospace Engineering, Anna University, Madras Institute of Technology campus, Chromepet, Chennai, 600044, Tamil Nadu, India
[2]Department Aeronautical Engineering, Rajalakshmi Engineering College, Thandalam, Chennai, 602105, Tamil Nadu, India
Corresponding author: Harish Soundararajan; Emails: harishaerophd@zoho.com; harish.s.aero@rajalakshmi.edu.in

Received: 8 October 2023; **Revised:** 23 July 2024; **Accepted:** 8 October 2024

Keywords: thrust vectoring; rocket nozzles; jet deflection; shock vectoring

Abstract

In this paper the performance of an internal strut-based thrust vector control (TVC) system has been studied at different expansion conditions of propulsion nozzle. The TVC system uses a cylindrical strut inserted through the diverging wall of a supersonic nozzle. This TVC system can be construed as an alternative to secondary injection TVC method. The nozzle had an expansion ratio of 1.545 and nozzle pressure ratio (NPR) of 6.61 for optimum expansion. Numerical simulations were performed at over-expansion (NPR = 3.94) and under-expansion (NPR = 7.89) conditions for four strut locations (x_s) and five strut heights (h_s). The strut location from the nozzle throat corresponded to 33%, 50%, 66.7% and 80% of the diverging length (L_d) of the nozzle. The schlieren images of the nozzle exhaust and nozzle internal wall pressure distribution from experiments were compared with the results from numerical simulation and the agreement was quite good. Computational results show that introduction of the strut caused a maximum total pressure loss of 1.5% at its maximum height. The calculations also show that ±4° thrust deflection angle could be achieved using combinations of strut location and strut height over a range of nozzle operational conditions. Thrust vectoring performance of strut insertion TVC was evaluated using a parameter called vectoring performance index (VPI) defined as thrust deflection angle per unit percentage of pressure loss. The maximum VPI was observed when $x_s = 0.5L_d$ at $\bar{h}_s = 0.429$ in both over-expansion and under-expansion conditions. The study reveals that an internal strut based TVC has a good future potential to be developed as an alternate TVC system obviating the requirement of carrying a fluid tank for a system like secondary injection TVC.

Nomenclature

Symbols

A	area (m)
d	diameter (m)
F	force (N)
h	height (m)
L_d	divergent Length (mm)
p	tatic pressure (Pa)
p_o	total pressure (Pa)
r	radius (m)
x_t	throat location (distance from nozzle inlet to nozzle throat)
$\bar{h}_s$	dimensionless strut height (h_s/r_t)
$\frac{(x-x_t)}{L_d}$	dimensionless strut location
δ	thrust deflection angle
η	vectoring performance index (deflection per unit total pressure loss)

Acronym

CD	convergent divergent
CSSW	counter strut side wall
GCI	grid convergence index
GGI	general grid interface
RANS	Reynolds average Navier Stokes
SST	shear stress transport
SSW	strut side wall

Subscript

w	nozzle wall surface
t	nozzle throat
e	nozzle exit
i	nozzle inlet
l	loss
s	strut
SSW	nozzle divergent wall surface below y=0 plane
CSSW	nozzle divergent wall surface above y=0 plane
ws	with strut
wos	without strut

Superscript

x,y,z	components of vector quantity
′(prime)	non-dimensional quantity

1.0 Introduction

Manoeuvrability of supersonic aircraft is commonly achieved by the control surfaces of vehicle airframe. However, this can also be supplemented by thrust vectoring, which is generally achieved by active mechanical thrust vector control (TVC) systems. Modern fighter aircraft already employ nozzles that can be used for thrust vectoring. In case of vertical take-off and landing (VTOL) aircraft, generally an entire engine can be gimballed for changing the direction of thrust for the purpose of VTOL. The performance of a TVC system and its weight significantly contribute to the overall success of the mission. Rocket propulsion-based space vehicles use either mechanical or fluidic TVC system or a set of reaction control system (RCS) nozzles or a combination of these to steer them at high altitudes and in space. A reduction in weight of TVC system yields either an increase in payload or a saving in launch cost. TVC systems are sometimes classified as single nozzle and multiple nozzle-based systems. Single nozzle-based systems have been operated using a variety of methods, examples being nozzle guide vanes, jet tabs, jet-evators, nozzle rings, swivel-nozzle and secondary injection etc. Rotation of entire thrust chamber is also possible when chamber size is not large. Fluidic thrust vector (FTV) control methods including secondary injection thrust vector control (SITVC) have been the most researched till date. SITVC system has been widely used for many space launch vehicles around the world. All FTV systems require fluid to be injected into the rocket nozzle, and thus fluid is to be carried separately in the launch vehicle. Some types of FTV control methods are injection of fluid (i) in the direction of flow (co-flow method), (ii) in the direction opposite to that of the flow (counter flow method) [1] (iii) in throat region (throat-shifting method) [2] and (iv) in the diverging section of nozzle (shock vectoring control method) [3, 4]. It is well known that in SITVC, the fluid is injected through the diverging wall into the supersonic cross flow of the nozzle. As a result, a bow shock wave is formed ahead of the injected jet. This shock wave alters the internal wall pressure distribution in the nozzle thus creating a side force. The

https://doi.org/10.1017/aer.2024.121 Published online by Cambridge University Press

basic features, operating principle, merits and limitations and the extent of research on SITVC is well documented in the literature [5, 6] and will not be elaborated here. However, it is observed that some fluid dynamic aspects of the SITVC have some common features with supersonic flow over solid objects which can be used for jet deflection and direction control. Examples include the old methods such as jet tabs [7, 8], recently the moving plate [9] and jet vanes [10]. The length of the flat wall attached at the nozzle exit was also found to affect direction of jet deflection [11]. Attempts were also made achieve vehicle flight control using pin protuberances on the blunt cones [12]. The high-pressure regions ahead of solid protuberance were used for steering the vehicle [13]. It was observed that protuberance geometry and Mach number significantly affect flow separation ahead of protuberance but Reynolds number had only a sobering effect on the separation [14]. Many researchers analysed the flow field around protuberances/struts in a cross flow with their major dimension perpendicular to the free-stream. This analysis was done by some researchers using nanoparticle based planar laser scattering method [15], wall pressure data [16], oil flow visualising [17] and yet others by using CFD simulation [18]. It was noticed that phenomena like upstream flow separation, spiral vortices near the wake of protuberance and horseshoe vortex system around the strut existed. It was proposed four decades ago that movable probe inserted into diverging wall of a rocket nozzle could perform the job of thrust vectoring [19] and could significantly contribute to weight reduction of space launch vehicle [20]. Solid strut-like objects were also used on the expansion ramp of scram jet thruster laboratory models to assess the thrust vectoring feasibility in the recent past [21]. Deflection of the ramp flow and additional side force development required for thrust vectoring was noticed [22]. Experiments were also conducted by inserting a square rod as probe/strut through the diverging wall of a supersonic nozzle perpendicular to nozzle axis to find out the feasibility of the strut insertion method as a thrust vectoring control technique [23] when the nozzle expanded optimally. Experiments were also carried out at non-optimum expansion conditions [24] by inserting the strut at different locations through the nozzle diverging wall. From the experimental data on nozzle wall distributions, it was descried that the side force and pitching moments varied alike with increase in strut height. A numerical study on a similar method was carried out in which a circular rod insertion perpendicular to diverging wall was used [25]. Numerical simulation showed that at optimum expansion combinations, depending upon strut height and strut insertion location, the strut insertion method could produce a thrust deflection ranging from $+4$ to -4°[26]. The present work is different from previous studies in several respects. The strut in this numerical study is of circular shape and inserted perpendicular to nozzle wall to explore thrust vectoring at non-optimum conditions of expansion. This contrasted with the experimental studies conducted by others using a square cross section strut inserted through the nozzle diverging wall perpendicular to nozzle axis at under-expansion conditions [23, 27]. Similar strut shape was used for experimental investigation but at over-expansion conditions by Ref. [24]. The CFD calculations in the present study were performed by varying the strut position from the nozzle throat over a wider range i.e., from $0.33L_d$ to $0.8L_d$ in contrast to other studies [25] wherein the strut position effect closer to nozzle throat was not investigated. Further, in the present study, the grid size near the nozzle and strut walls was much smaller (0.0005 mm) than the one used in Ref. [25] which was 0.01 mm. In the present investigation, exhaust jet trajectories and jet deflections were obtained and performance analysis of thrust vectoring was conducted at non-optimum conditions of expansion in contrast to the other study [26] which was confined to the analysis at optimum expansion condition.

Figure 1 shows flow features inside a converging-diverging (C-D) nozzle with internal strut. When the supersonic flow encounters a solid object such as a strut, it creates a bow shock wave. The bow shock and separation shock ahead of the strut form a lambda shock system on strut side wall (SSW). On the counter strut side wall (CSSW) the shock impinges, raising the wall pressure. The pressure imbalance between SSW and CSSW creates net side force on nozzle which would be used to control the vehicle. The internal strut based TVC method can be used as an alternative technique for SITVC in space launch vehicles wherein thrust vectoring is needed frequently for long operational times. The strut based TVC can be used with advantage because the requirement of carrying a fluid tank can be dispensed with. This reduces overall weight and space requirements. In the present paper, an overall performance study of such an alternative TVC system was undertaken using CFD simulation. Some preliminary experiments

https://doi.org/10.1017/aer.2024.121 Published online by Cambridge University Press

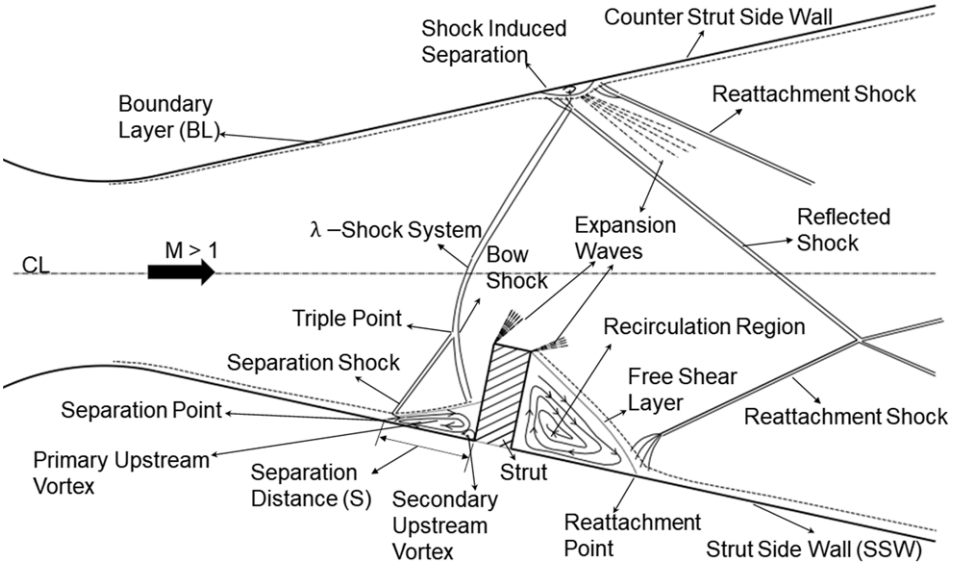

Figure 1. *Schematic of flow field inside C-D nozzle with strut insertion [26].*

were also conducted to validate the CFD results. The important operational parameters considered were strut height (h_s) and strut location (x_s). The performance assessment was done at both low altitude (over-expansion) and high altitude (under-expansion) conditions of the nozzle.

2.0 Experimentation

2.1 Description of experimental facility

Experiments were conducted for obtaining nozzle wall pressure (p_w) distributions using high-speed jet facility in department of Aerospace Engineering, Anna University at MIT campus (Chennai). The air supply system of the facility consists of a compressor and a storage tank. A three-phase induction motor drives the compressor delivering air at 3.5 MPa to storage tank through a filter and drier. The facility also consists of settling chamber, pressure regulating valve and nozzle mounting flange. The pressure regulator maintains required constant total pressure in the settling chamber. The nozzle back pressure was the ambient pressure to which the jet was to discharge. The ambient (laboratory) pressure was measured using a barometer and was found to be 99.95 kPa.

A schematic layout of experimental facility is shown in Fig. 2. The nozzle wall pressure measurements were made using 9,116 intelligent pressure scanner with 16 channels supplied by Measurement Specialties USA. The pressure scanner has ± 0.05% accuracy [28]. Pressure in each channel was recorded at rate of 500 sample per second. External flow field characteristic was studied using schlieren imaging. The purpose of this limited experimental study is to compare some of the results obtained from CFD simulations.

2.2 Nozzle geometry and dimensions

Experiments were conducted on a C-D nozzle with circular arc throat connecting convergent and diverging section of the nozzle. The area ratio and exit Mach number of the nozzle were 1.545 and 1.89, respectively. The dimensions of nozzle are shown in Fig. 3.

The semi-divergent angle of nozzle was 2.6°. The diverging section length (L_d) was 40mm. The nozzle has a provision for insertion of strut at $x_s = 0.5L_d$ through which the strut is inserted using a strut

https://doi.org/10.1017/aer.2024.121 Published online by Cambridge University Press

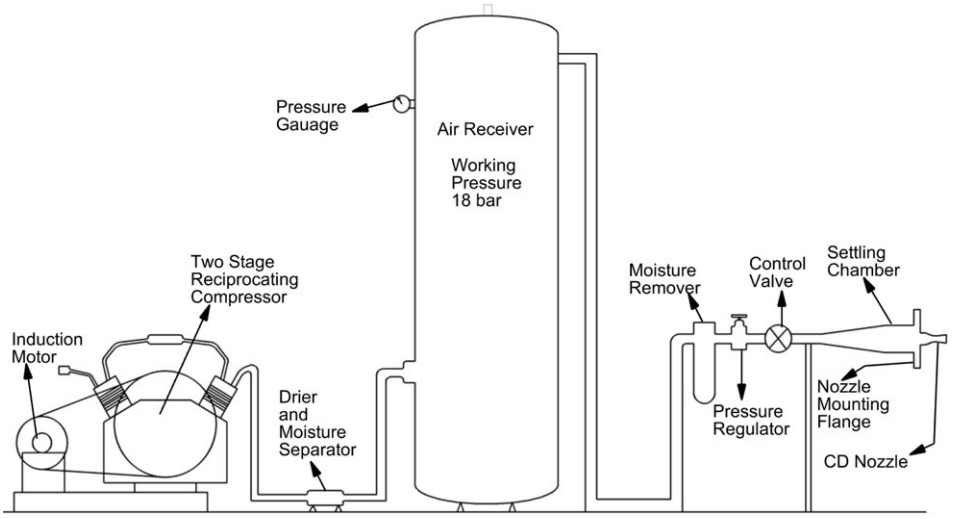

Figure 2. *Schematic of high-speed jet experimental facility.*

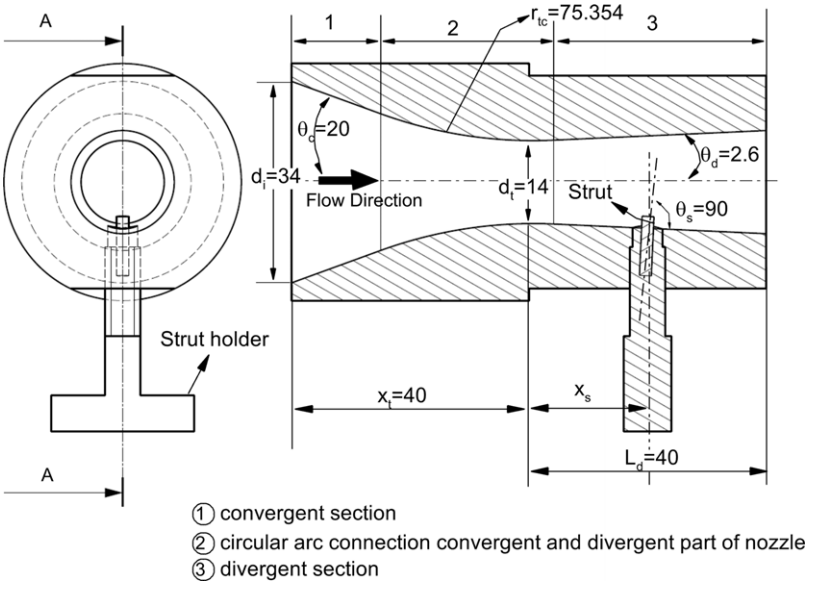

Figure 3. *Nozzle geometry with strut holder arrangement.*

holder. The strut holder surface has same profile as nozzle at strut holder insertion point. To measure the p_w distribution, 12 pressure tapings on strut side wall (SSW) and counter strut side wall (CSSW) were made. The diameter of pressure tapping was 0.4 mm, and the strut was screwed into the strut-holder and inserted into the strut insertion hole. The photograph of experimental facility with nozzle fixing is shown in Fig. 4.

3.0 Numerical analysis

To get a detailed insight of flow field and performance evaluation of strut insertion-based TVC, CFD analysis was carried out. The analysis at two NPRs corresponding over-expansion (NPR = 3.94) and

https://doi.org/10.1017/aer.2024.121 Published online by Cambridge University Press

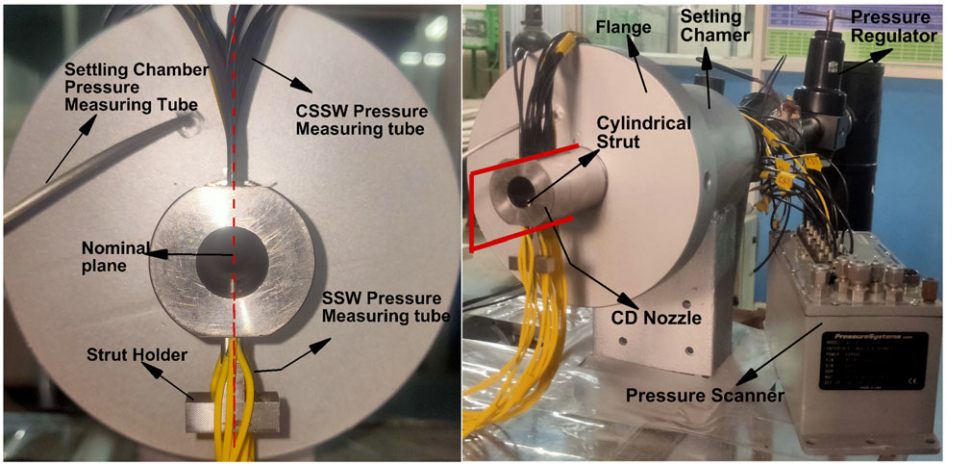

Figure 4. *C-D nozzle with strut mounted on experimental setup.*

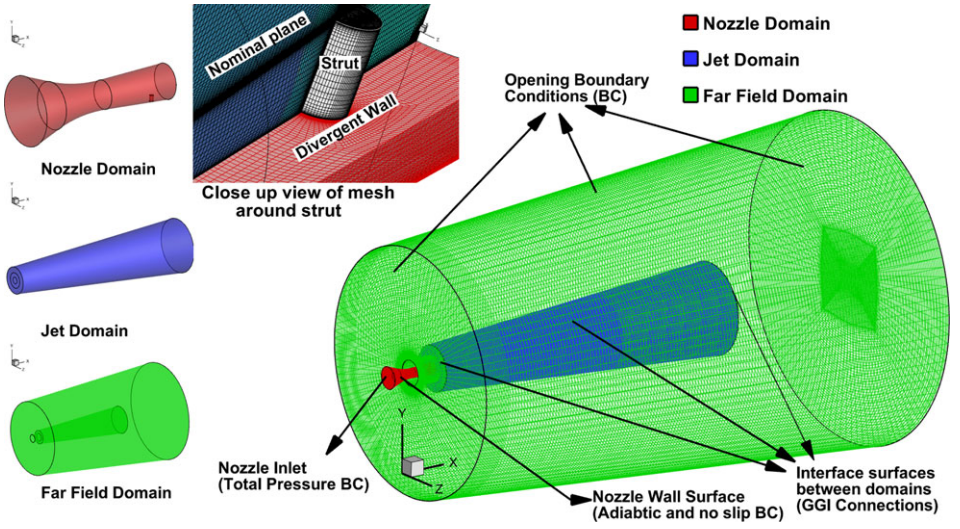

Figure 5. *Computational domain, boundary condition and mesh.*

under-expansion (NPR = 7.89) conditions was made using Ansys CFX software [29]. In this section, the details of computational domain, meshing method and verification of computational results with sample experimental data pertaining to thrust vectoring will be discussed.

3.1 Computational domain, meshing and boundary conditions

The computational domain consisted of three separate mesh domains as shown in Fig. 5. These three domains were the nozzle domain, jet domain and far field domain. The nozzle domain covered flow inside the nozzle. To capture the nozzle exhaust jet flow structure, a separate domain called jet domain was used. In this jet domain fine spacing between the grid points was ensured. This domain extends from nozzle exit to 28 D_e. The far field domain extends to 45 D_e in axial direction and 28 D_e in radial direction. These three domains were separately loaded into Ansys CFX and connected using a general grid interface (GGI) tool. At the nozzle inlet, total pressure and total temperature were specified. On the

https://doi.org/10.1017/aer.2024.121 Published online by Cambridge University Press

Table 1. *Grid independence study solution details*

Mesh	Fine Mesh (f_1)	Medium Mesh (f_2)	Coarse Mesh (f_3)	Relative Error ε_{23} (%)	Relative Error ε_{12} (%)	GCI_{23} (%)	GCI_{12} (%)
F_x *(N)*	59.93	59.92	59.79	0.22	0.01	0.71	0.04
F_y *(N)*	3.65	3.64	3.29	9.44	0.28	29.17	0.87
$p_{o\ out}$ *(kPa)*	347.69	347.42	345.46	0.56	0.08	1.96	0.27

outer surface of far field domain, the opening boundary condition [29] was specified with a laboratory pressure of 99.95 kPa.

The structured mesh domains were created in ICEM CFD [30]. The total number of elements in the three domains was around 6 million. The numerical study was carried using SST turbulence model which requires $y^+ < 1$, and the first cell height was about $0.5\ \mu m$ away from the wall. The SST turbulence model is known to give better results for flows with strong adverse pressure gradients when compared to those obtained with either the original $\kappa-\epsilon$, or $\kappa - \omega$ models [31]. The wall pressure distribution in the nozzle diverging section is strongly affected by the presence of the strut, which would cause adverse pressure gradients and exhaust jets are of free shear region. Hence the selection of SST turbulence model is a fair choice as it combines advantages of $k-\omega$ near walls and $k-\epsilon$ in wakes and free-shear flow regions [32] and the model is expected to give reasonably good results for the computational work done in this paper. Grid point distributions for three separate domains and around cylindrical strut are shown in Fig. 5. Working medium was air with ideal gas assumption. Specification of nozzle inlet conditions included total pressure, temperature (300 K) and turbulence intensity level of 5%. Nozzle walls were considered no-slip and adiabatic walls. The opening boundary condition was specified on the outer surface of the far field domain with opening pressure and temperature of 99.95 kPa and 300K, respectively.

3.2 Grid independence study

Optimal grid size for the numerical analysis was found by performing grid independence test on three meshes (1 Fine, 2 Medium and 3 Coarse) in the nozzle with the strut located at $0.8L_d$ with dimensionless strut height ($\bar{h_s} = 2h_s/d_t = 0.429$) and diameter 2 mm, at NPR 3.94. The total number of elements in the jet and far field domains were kept constant; only the number of elements in nozzle alone varied from 0.25 million for coarse to 4.1 million for fine mesh. Maximum elements size for Fine Mesh, Medium Mesh and Coarse Mesh were 0.2, 0.33 and 0.55 mm, respectively. To properly capture the boundary layer near the wall 22 grid points was used with growth factor of 1.15. The refinement ratio (r) for Coarse Mesh to Medium Mesh and Medium mesh to Fine Mesh were 1.6. The order of convergence (p) was obtained by using the relation $ln\left((f_3 - f_2)\ /\ (f_2 - f_1)\right)\ /\ln(r)$ where $f_1, f_2\ and\ f_3$ were solution quantities from Fine, Medium, and Coarse Mesh, respectively [33].

The grid convergence index for solution quantities such side force, axial and total pressure were obtained and given in Table 1. Wall pressure distributions on *SSW* and *CSSW* show only small variations near the strut and this variation also decreases as mesh is refined to Fine Mesh having 4.1 million cells as shown in Fig. 6. Hence the present CFD analysis was done using Fine Mesh with SST turbulence model.

3.3 Thrust vectoring performance variables

Performance of strut insertion-based TVC system was evaluated using the various parameters described in this section. In Ref. [26] performance analysis for optimum expansion condition (NPR = 6.61) was done. In this section the analysis is for over-expansion and under-expansion conditions.

https://doi.org/10.1017/aer.2024.121 Published online by Cambridge University Press

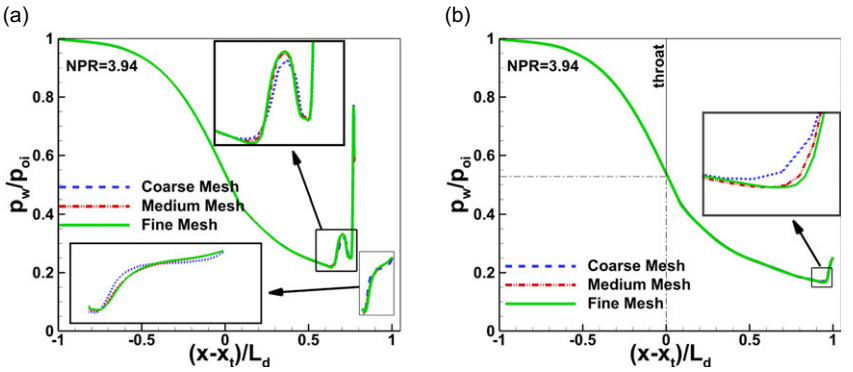

SSW pressure distributions. *CSSW pressure distributions.*

Figure 6. *Wall pressure distributions under grid independence studies. $\bar{h_s} = 0.429$ with strut located at 0.8 L_d and NPR = 3.94.*

3.3.1 Calculations of forces

The force was obtained using relation [26]

$$\vec{F} = -\iint_A (p - p_\infty)\,\overrightarrow{dA} + \iint_A \vec{V} d\dot{m} \tag{1}$$

$d\dot{m}$ is the small mass flow rate passing normal to the small area dA on-outlet surface A, p_∞ is the back pressure acting on the nozzle exit plane, $\int \vec{V}\, d\dot{m}-$ momentum flux through outlet surface A. As the z-component force F^z is of the order of 10^{-4} N, only the x-component force F_x and y-component force F_y (or the vehicle side force) were considered for the performance evaluation.

3.3.2 Nondimensionalised force (F')

It is the ratio of the force F to the product of the nozzle inlet total pressure (p_{oi}) and the nozzle throat area (A_t) [26].

$$F' = \frac{F}{p_{oi} A_t} \tag{2}$$

3.3.3 Thrust deflection angle (δ)

It is the ratio of the vehicle side force (F^y) to the axial component of thrust ($-F^x$) [26].

$$\delta = \tan^{-1}\left(\frac{F^y}{F^x}\right) \tag{3}$$

It is the angle between thrust axis and nozzle axis and is measured from nozzle axis. δ when measured in anticlockwise and clockwise directions is taken as negative and positive respectively. Upward and downward vehicle side forces were treated as positive and negative respectively.

3.3.4 Nondimensionalised thrust loss (T_l' in%)

It is the ratio of the resultant force generated by the nozzle with the strut to the force generated by the nozzle without a strut at a given nozzle pressure ratio and is expressed as a percentage [26].

$$T_l' = 1 - \left(\frac{\left(\sqrt{(F^x)^2 + (F^y)^2}\right)_{ws}}{F^x{}_{wos}}\right).100 \tag{4}$$

since $F^y = 0$ for without strut

https://doi.org/10.1017/aer.2024.121 Published online by Cambridge University Press

3.3.5 Nondimensionalised total pressure loss (p'_{0l})

It is the ratio of total pressure loss from inlet to outlet across the nozzle length with strut to that without strut, at given NPR [26].

$$p'_{0l} = \frac{(p_{oi} - p_{oe})_{ws}}{(po_i - p_{oe})_{wos}} \tag{5}$$

where $(p_{oi} - p_{oe})_{ws}$ is the difference in total pressures between inlet and exit of the nozzle with strut insertion for any given strut height and strut position and $(po_i - p_{oe})_{wos}$ is the total pressure difference without strut insertion.

3.3.6 Vectoring performance index (η)

It is the magnitude of thrust vector deflection angle obtained using the strut per unit total pressure loss. This represents the vectoring performance index (VPI) of the strut insertion method [26].

It is independent of size of TVC system but depends on strut inclination angle, strut location and flow conditions upstream of the strut.

$$\eta = \left(\frac{|\delta|}{p'_{0l}}\right) \tag{6}$$

4.0 Results and discussion

4.1 Computational validation

To verify the computational results, experiments were performed in a high-speed jet facility using C-D nozzle with cylindrical strut located at *0.5 L_d*. Schlieren images of the supersonic exhaust jet from the nozzle with $\bar{h}_s$ of 0.714 located at $x_s = 0.5\ L_d$ for two NPRs (3.94 and 7.89) were shown in Fig. 7. The shock structure obtained from experimental schlieren images (both X-density and Y-density gradient images obtained by keeping the knife edge position vertically and horizontally, respectively) matches well with the numerically obtained shock structure in the nominal plane (see Fig. 4). Both experimental and numerical images show that insertion of strut causes appreciable deflection of jet. Numerical schlieren image shows the internal flow field structure that has a carry-over effect on the shock structure in the supersonic exhaust stream.

The *SSW* and *CSSW* distributions of p_w obtained from experiment were compared with CFD results in Fig. 8. It can be noticed from the figure that the agreement between them is good. The uncertainties in the experimental data were very small and difficult to be represented by error bars in the pressure plots of the data. For example, a value of 0.4 in the y-axis of the Fig. 8, may have an uncertainty ranging from 0.4004 to 0.3996 (for NPR = 3.94), which was quite tough to represent by way of error bars, as the reasonable symbol size itself would be larger than the error bar. Hence error bars were avoided for the experimental data in Fig. 8.

4.2 Exhaust jet shock structure

In the following paragraphs, the numerically obtained density gradients in the nominal plane at both over-expansion (NPR = 3.94) and under-expansion (NPR = 7.84) conditions are presented (Figs 9, 10, 11 and 12). This is given at minimum ($\bar{h}_s = 0.142$) and maximum ($\bar{h}_s = 0.714$) strut heights at different strut locations. The jet boundary is also marked in these figures. The supersonic core region is the flow field inside the *M = 1* contour line. The dot and dashed line is the nozzle geometrical centre line. The bold solid line is the calculated midline from jet boundary. The jet boundary in the nominal plane was defined as the locus of the point at which the flow velocity is 5% of maximum velocity in the local velocity profile, i.e. V(y) at any $(x\text{-}x_e)/d_e$.

Figure 9 shows the shock structure at $x_s = 0.33\ L_d$. The shock pattern inside the nozzle and in the exhaust jet are presented in Fig. 9(a) for over-expansion and in Fig. 9(b) for under-expansion conditions.

https://doi.org/10.1017/aer.2024.121 Published online by Cambridge University Press

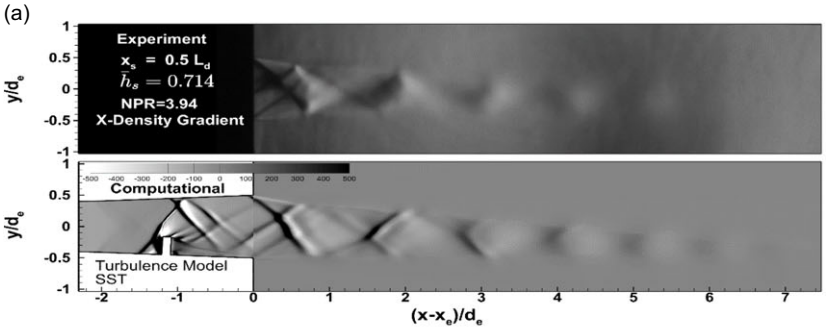

X density gradients at NPR = 3.94.

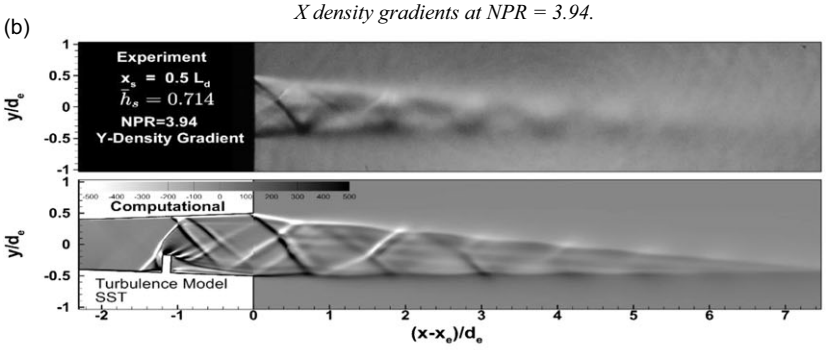

Y density gradients at NPR = 3.94.

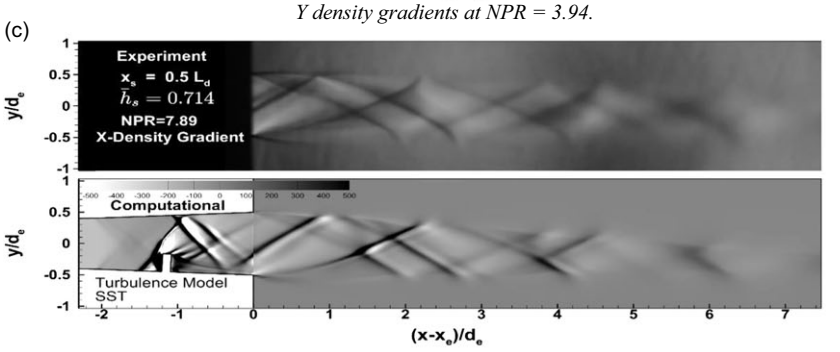

X density gradients at NPR = 7.89.

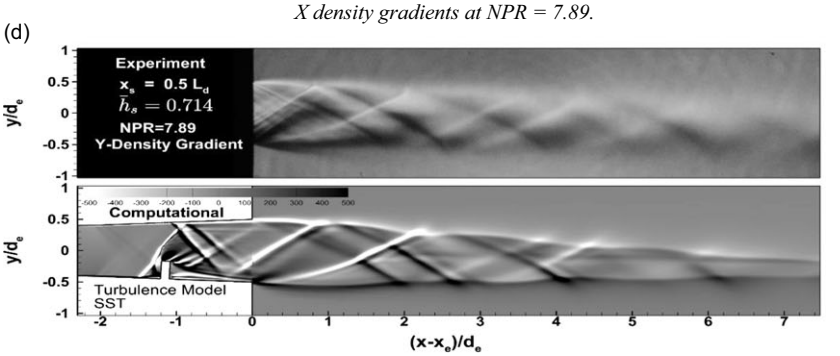

Y density gradients at NPR = 7.89.

Figure 7. *Validation of experimental and numerical schlieren images for strut height ($\bar{h}_s$) = 0.714, located at 0.5 L_d.*

https://doi.org/10.1017/aer.2024.121 Published online by Cambridge University Press

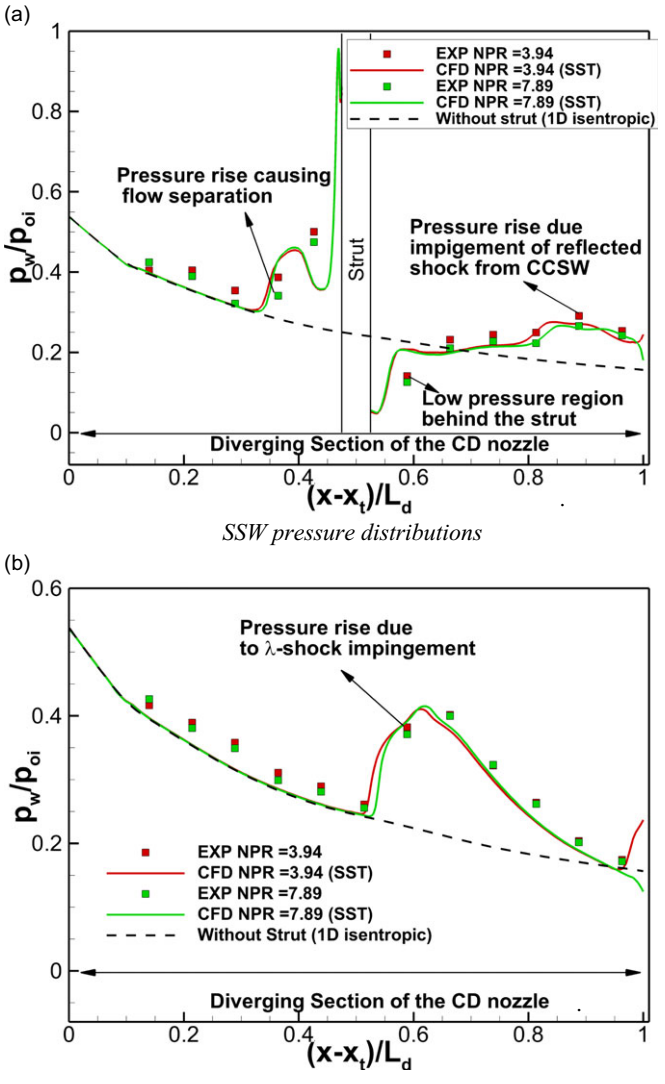

Figure 8. *Experimental and numerical wall pressure distributions comparison for strut height* $(\bar{h_s}) = 0.714$*, located at 0.5* L_d.

An upward jet deflection could be noticed at large strut heights ($\bar{h_s} = 0.714$) and a downward deflection at small heights ($\bar{h_s} = 0.142$). Similar shock patterns were presented in Fig. 10 for both the expansion conditions at $x_s = 0.5\ L_d$. However, it can be espied from the figure that at this strut location the jet deflection was always downward for both small and large strut heights.

The jet deflection behaviour with strut height changes when the strut location is farther from the nozzle throat to exit, i.e. at $x_s = 0.667\ L_d$ (Fig. 11). A noticeable downward jet deflection could be seen at large strut heights at under-expansion conditions. In contrast to $x_s = 0.5\ L_d$ case, the jet deflection was upward for both small and large strut heights when strut was positioned far away from the nozzle throat, i.e. $x_s = 0.8\ L_d$ (Fig. 12). The upward jet deflection exists for both over-expansion and under-expansion conditions.

It can be noticed from the shock structures in the nozzle diverging section of Figs 9, 10, 11 and 12 that small h_s would generate more obliquity to the detached shock standing in front of the strut. As a result,

https://doi.org/10.1017/aer.2024.121 Published online by Cambridge University Press

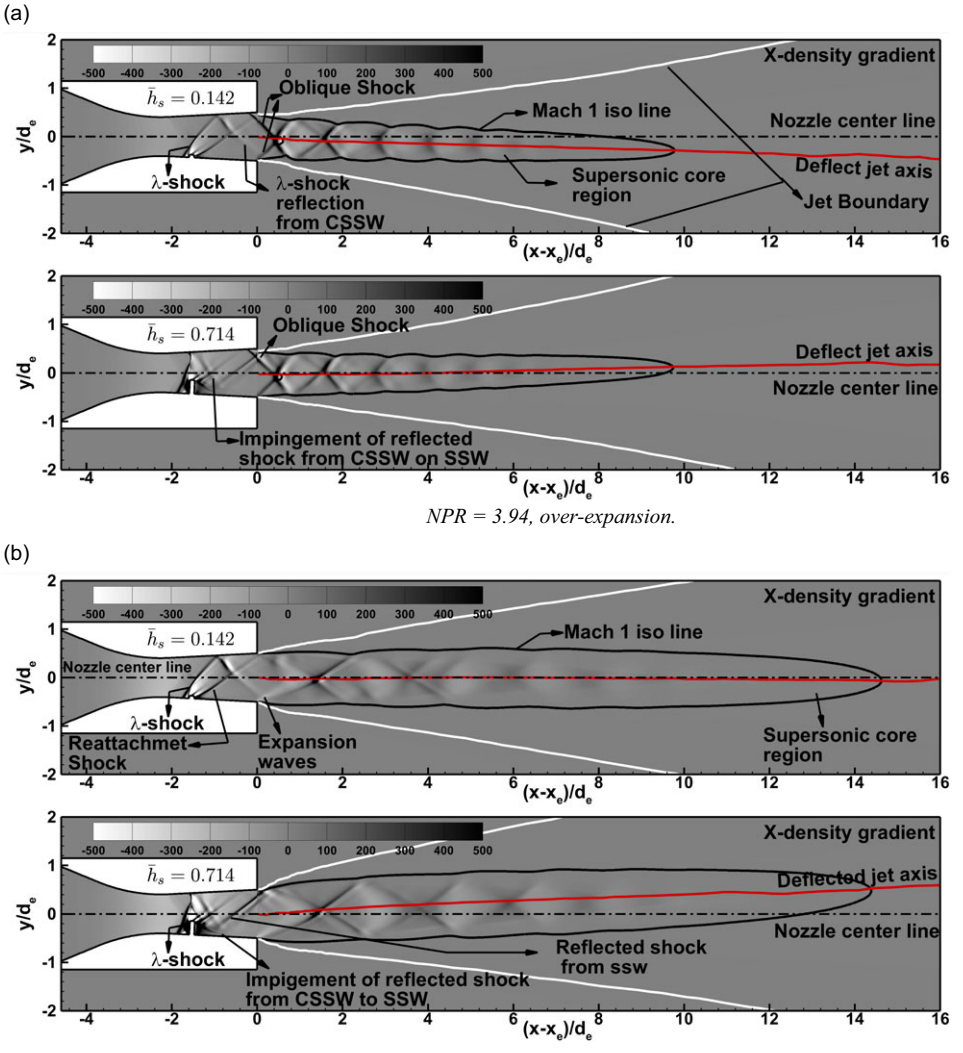

Figure 9. *Jet shock structure due strut insertion at 0.33 L_d.*

the oblique shock generated by the small h_s would impinge CSSW closer to the nozzle exit in contrast to the less oblique shock generated by the larger h_s, which impinges the CSSW somewhat farther from the nozzle exit. In fact, it can be noticed from Figs 11 and 12 that the CSSW of the nozzle escapes the impingement from the shock generated by the small h_s for the strut locations $x_s = 0.667\ L_d$ and $0.8\ L_d$. This would alter the nozzle wall pressure distribution on both SSW and CSSW sides and determine the side force eventually.

4.3 Side force coefficient variation with dimensionless strut height

The internal wall pressure distribution of the entire nozzle section was integrated with respect to nozzle wall surface and was resolved in Y-direction (normal to nozzle axis) to find out the magnitude of the side force generated as a result of strut insertion. This was done for all $\bar{h}_s$ and x_s at both over-expansion (NPR = 3.94) and under-expansion (NPR = 7.94) conditions. These results have been shown

https://doi.org/10.1017/aer.2024.121 Published online by Cambridge University Press

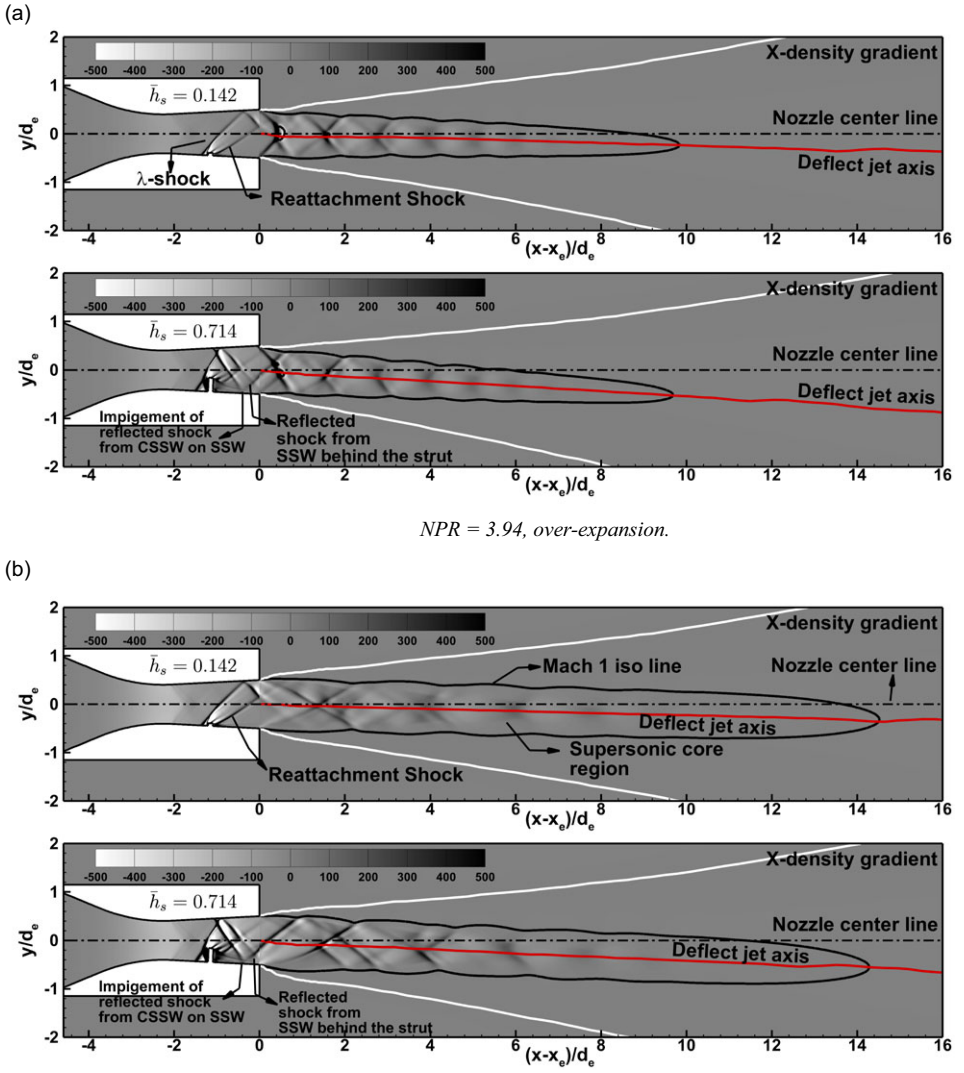

NPR = 3.94, over-expansion.

NPR = 7.89, under-expansion.

Figure 10. *Jet shock structure due srtut insertion at 0.5 L_d.*

in Fig. 13. In these figures x-axis represents $\bar{h}_s$ whereas y-axis represents side force coefficient ($F^{y'}$), i.e. dimensionless vehicle side force.

The upward vehicle side force was taken as positive and in combination with axial component of thrust force produces a resultant thrust vector inclined to nozzle axis at an angle δ. The upward side force produces a pitch-down moment on the vehicle in the anti-clock wise direction. The inclination angle, which is the vectoring angle (δ) measured from nozzle axis to thrust vector, is treated as positive when measured in clockwise direction. The downward vehicle side force is treated as negative and in vector combination with the axial component of thrust force gives a thrust vector which is again inclined to the nozzle axis. The negative side force produces a pitch up moment. The angle δ measured in the anti-clock wise direction from the nozzle axis to the thrust vector is treated as negative.

An upward side force is produced when the integrated pressure force on the upper half (CSSW section) of the nozzle internal surface exceeds its counterpart on the lower half (SSW section). High-pressure regions on CSSW of the nozzle exist due to incident shocks, and low-pressure regions are also

https://doi.org/10.1017/aer.2024.121 Published online by Cambridge University Press

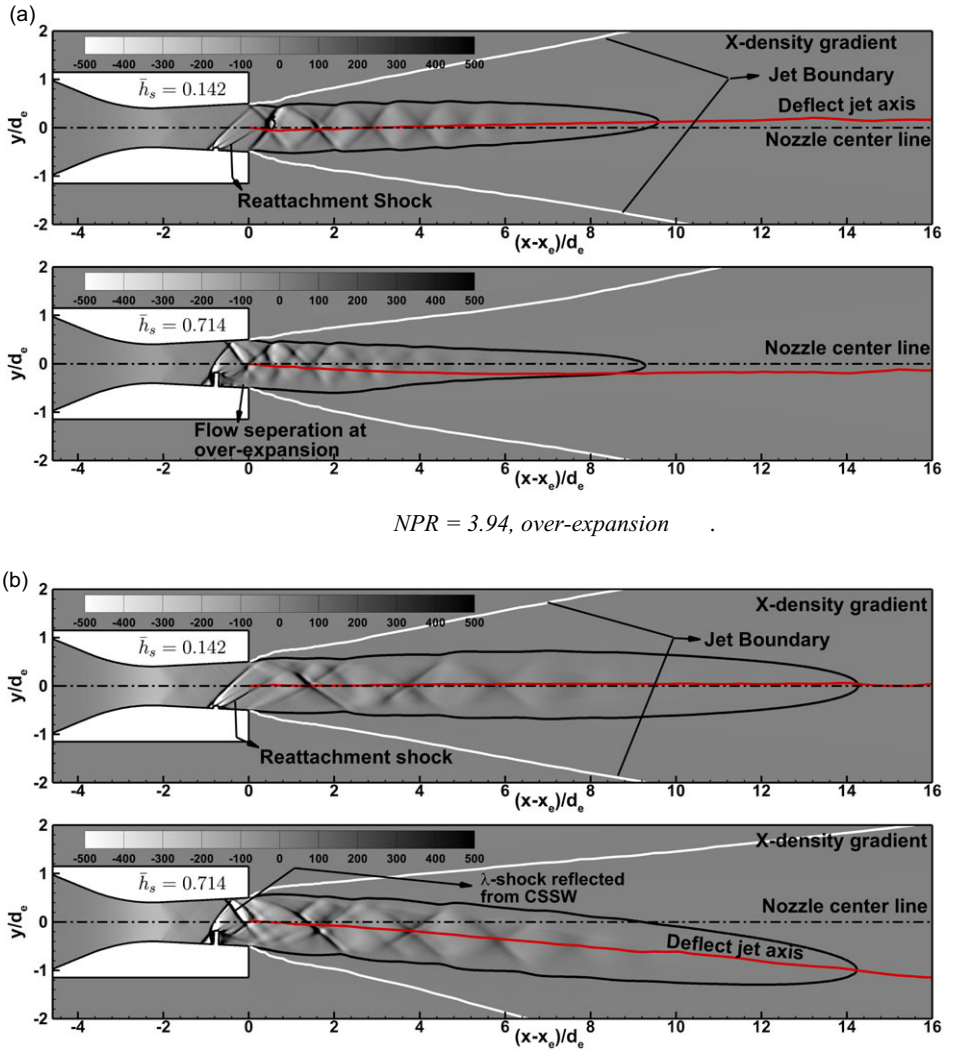

Figure 11. *Jet shock structure due strut insertion at 0.667 L_d.*

formed due to boundary layer separation. The SSW of the nozzle also experiences high pressure due to the presence of separation shock, bow shock and reattachment shock but also has low-pressure regions due to flow separation in front of the strut and to recirculation behind it. The magnitude of integrated pressure force normal to nozzle axis is influenced by the strength of the shocks interacting with the wall and the size of the separation regions. Again, these fluid dynamic phenomena depend strongly on $\bar{h}_s$ and x_s. Hence one can deduce that the net outcome of the magnitude and direction of side force (normal to nozzle axis, i.e. Y direction) is determined by a complex play of the above interactions in the flow field. Some of the observations on the magnitude and direction of the side force influenced by $\bar{h}_s$ and x_s have been explained in Fig. 13. It can be seen in both Fig. 13(a) and (b) that the strut position (x_s) at $0.8L_d$ produced negative side force (downward) at all $\bar{h}_s$. It indicates that the SSW section of the nozzle internal surface experienced larger integrated pressure force when compared to the CSSW section did. This was mainly because of the strut position. At both over-expansion and under-expansion conditions, the separation shock produced on the SSW in front of the strut did not impinge on CSSW because of

https://doi.org/10.1017/aer.2024.121 Published online by Cambridge University Press

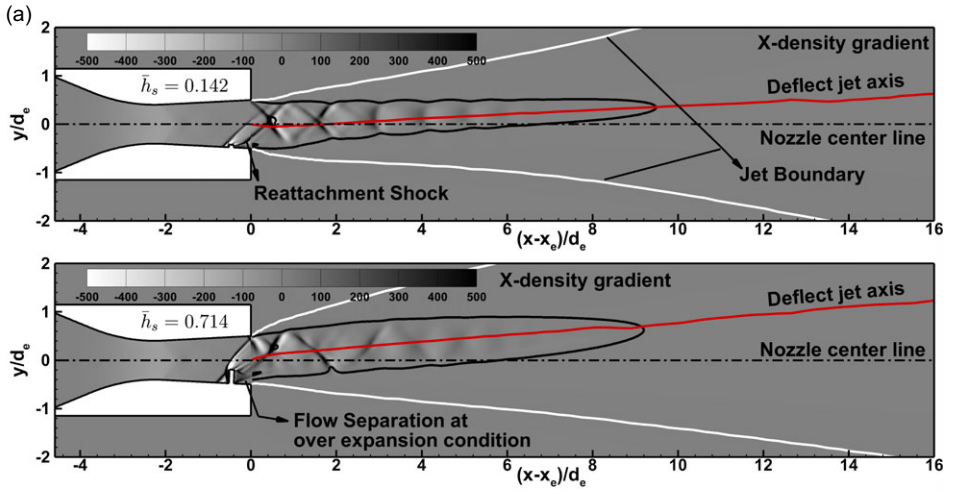

NPR = 3.94, over-expansion.

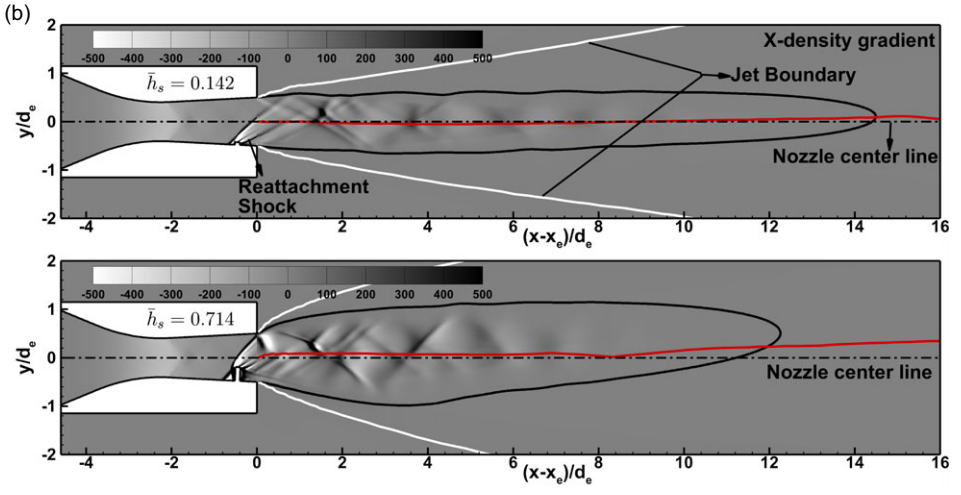

NPR = 7.89, under-expansion.

Figure 12. *Jet Shock structure due strut insertion at 0.8 L_d.*

the closer distance of the strut to nozzle exit and also due to shock obliquity especially at lower $\bar{h}_s$. As a consequence, the absence of shock impingement rendered CSSW experience smaller integrated wall force normal to nozzle axis in comparison to SSW. However, x_s =0.5 L_d position caused a positive side force, i.e. upward side force at both over-expansion and under-expansion conditions at all $\bar{h}_s$. This was because of the presence of high-pressure region on CSSW due to separation shock impingement. Though there was a rise in wall pressure across the separation shock on SSW, there were also low-pressure regions in front of the strut and also behind it. The net effect was that the asymmetric wall pressure distributions on SSW and CSSW created an imbalance of forces such that the net side force was upward. The magnitude of this side force increased with increase in $\bar{h}_s$ up to $\bar{h}_s$ =0.429. After this $\bar{h}_s$, the magnitude of upward side force decreased which could be due to the increased pressure behind the strut on SSW due to reflected shock impingement from CSSW (refer Fig.10(a) and (b) for $\bar{h}_s = 0.714$). At smaller $\bar{h}_s$, the impinging shock did not reach the nozzle SSW and hence causing no SSW pressure rise. Hence after $\bar{h}_s$= 0.429, the magnitude of side force continued to decline though remained positive and

https://doi.org/10.1017/aer.2024.121 Published online by Cambridge University Press

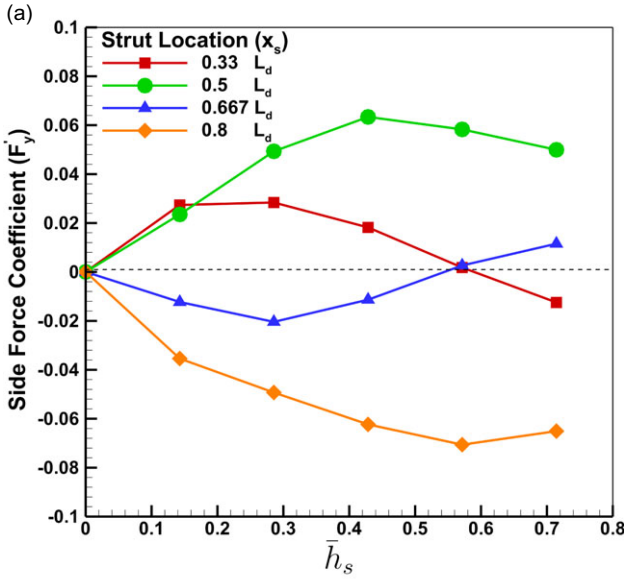

NPR = 3.94, over-expansion.

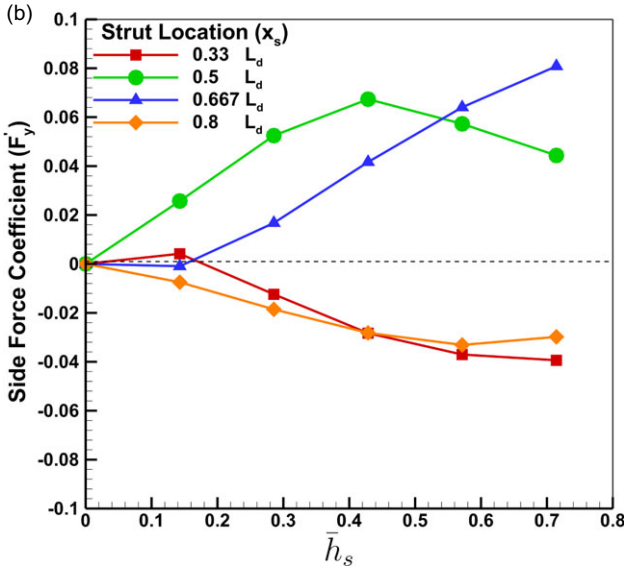

NPR = 7.89 under-expansion.

Figure 13. *Variation of side force coefficient with strut height, strut location and NPRs.*

upward. When the strut insertion was at x_s =0.33 L_d, the behaviour of the side force variation with $\bar{h}_s$ at over-expansion condition was different from that at under-expansion condition. From Fig. 13(a), it can be espied that at over-expansion condition, the side force was upward and increased with $\bar{h}_s$ up to $\bar{h}_s$=0.286 and thereafter declined. It almost became insignificant at $\bar{h}_s$ =0.571 and a further increase in $\bar{h}_s$ produced a negative side force, i.e. a downward force. In contrast, at under-expansion conditions, the side force generated was very little at small $\bar{h}_s$. However, when $\bar{h}_s$ was increased further, the side force exhibited a downward trend and the magnitude of the downward side force continued to increase

https://doi.org/10.1017/aer.2024.121 Published online by Cambridge University Press

with increase in $\bar{h}_s$. From the CFD simulation it was observed that at this strut location ($x_s = 0.33L_d$), the pressure distribution on SSW played an important role in determining the magnitude and direction of side force. At over-expansion conditions, it can be seen in Fig. 9(a) that an oblique shock on CSSW near the nozzle exit was present at both small and large $\bar{h}_s$ in addition to the impinging separation shock originating from SSW. Presence of both these shocks gave rise to high pressure regions on CSSW. However no significant flow separation regions were present on CSSW behind these shocks. It can also be observed from Fig. 9(a) that the oblique shock near the nozzle exit and the reflected shock arising out of impingement of separation shock from CSSW did not reach SSW. Further, no oblique shock on SSW near the nozzle exit could be observed which could be due to the presence of the strut. Flow separation regions on SSW could be observed for all $\bar{h}_s$. These features favoured an imbalance of wall forces in upward direction generating an upward side force. However, when $\bar{h}_s$ was increased beyond 0.286, the strength of separation shock in front of the strut increased resulting a decrease in the imbalance of wall forces perpendicular to nozzle axis. This contributed to a decline in the magnitude of upward side force and at $\bar{h}_s = 0.571$, the side force magnitude became very small indicating almost an equal magnitude of wall forces in upward and downward directions. A further increment in $\bar{h}_s$ tilted the imbalance in downward direction due to the impingement of reflected shock on SSW with a rise in wall pressure (refer to Fig. 9(a)). However, in comparison, at under-expansion conditions, at a given $\bar{h}_s$ no oblique shock formation was observed either on SSW or on CSSW near the nozzle exit (refer to Fig. 9(b)). The side force entirely depended on the shock structure well inside the nozzle. At $\bar{h}_s = 0.142$, the reflected shock from CSSW moved out of the nozzle exit without hitting SSW, hence a small upward side force was generated. When $\bar{h}_s$ was increased, the reflected shock from CSSW impinged on SSW behind the strut at all $\bar{h}_s$(refer to Fig. 9(b) for $\bar{h}_s = 0.142$ and $\bar{h}_s = 0.714$). The flow had a propensity to accelerate more over CSSW and had a somewhat restrained effect on the magnitude of wall pressure rise (due to shock impingement). Hence at under-expansion condition, a rise in $\bar{h}_s$ resulted in a larger integrated force on SSW than on CSSW such that the direction of imbalance of SSW and CSSW forces was in downward Y direction.

When the strut insertion distance was doubled from $x_s = 0.33\ L_d$ to $x_s = 0.667L_d$, the side force variation with $\bar{h}_s$ exhibited an opposite trend at over-expansion condition (Fig. 13(a)). With increase in $\bar{h}_s$ the side force exhibited a downward trend and reached a minimum at $\bar{h}_s = 0.286$. Up to this height, the separation shock impingement on CSSW had only little effect in rising the wall pressure and the impingement was closer to nozzle exit. As a result, the CSSW did not experience any significant pressure rise, however the wall pressure on SSW was relatively high due to the flow crossing the separation shock in front of the strut. With the further increase in $\bar{h}_s$ the downward side force magnitude decreased and reached a negligible value at $\bar{h}_s = 0.571$. During this increment, the strength of the separation shock (shock angle) increased and so its ability to impinge strongly on CSSW side. Separation shock impingement on CSSW side was favourable to engender an upward side force. Low wall pressure regions on SSW owing to boundary layer separation (refer to Fig. 11(a)) and recirculation in the vicinity of the strut also had a noticeable presence. The combined effect of shock impingement on CSSW and low-pressure regions on SSW had prompted this decline of downward side force. It can be further observed from Fig. 13(a) that an additional increment in $\bar{h}_s$ to 0.714 produced a small upward side force, indicating that shock impingement on CSSW and flow separation on SSW became favourable features to bring about an upward side force at this strut height (refer to Fig. 11(a)). It can be observed from Fig. 13(b) that at under-expansion conditions, at this strut location ($x_s = 0.667L_d$) very small $\bar{h}_s$ had a very diminutive effect on side force. However, an increase in $\bar{h}_s$ had resulted an upward side force that increased linearly with $\bar{h}_s$. When compared to over-expansion conditions, the separation shock impingement on CSSW occurred somewhat farther from the nozzle exit and the size of the separation region on SSW was also smaller. These features produced a larger integrated wall force on CSSW side when compared to that on SSW side, resulting an upward side force. The imbalance of CSSW and SSW side wall forces increased favourably towards CSSW side with increase in $\bar{h}_s$ and this variation was observed to be linear.

https://doi.org/10.1017/aer.2024.121 Published online by Cambridge University Press

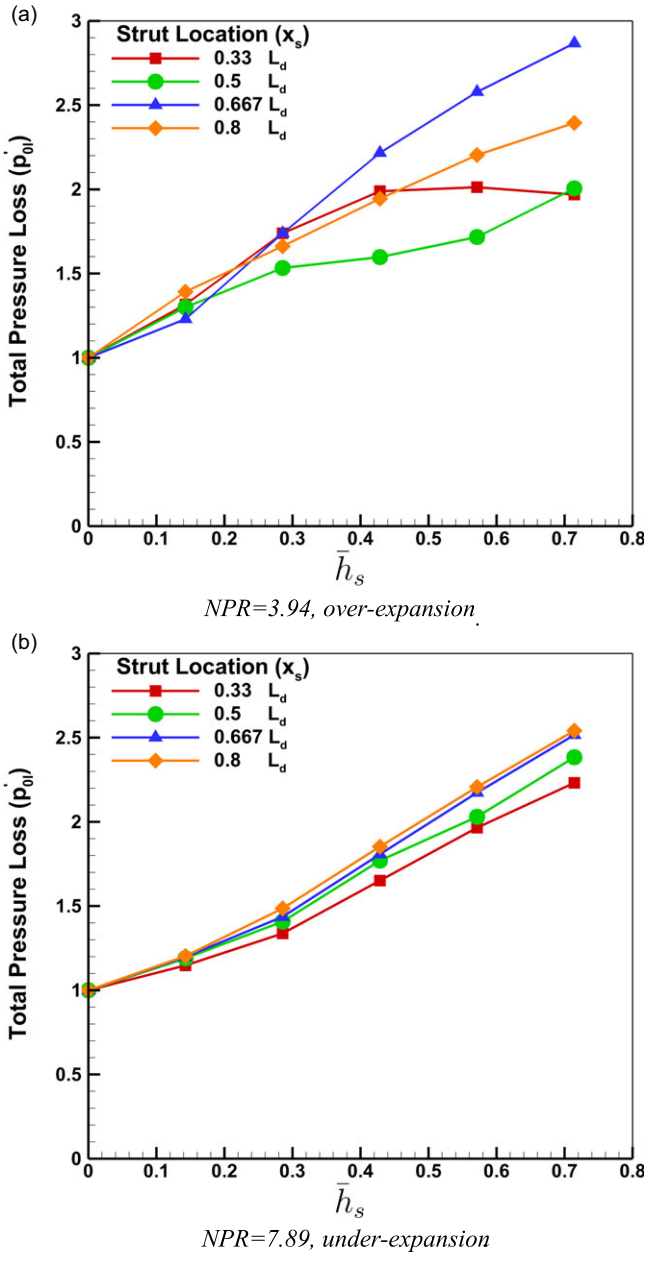

Figure 14. *Variation of total pressure loss with strut height, strut location and NPRs*

4.4 Total pressure loss and thrust loss with strut height

The dimensionless total pressure loss (p'_{ol}) was plotted against dimensionless strut height $\bar{h}_s$ at NPR = 3.94 in Fig. 14(a) and at NPR = 7.89 in Fig. 14(b) with strut location (x_s) as the parameter. In over-expansion conditions (NPR = 3.94), the strut location $x_s = 0.667\ L_d$ caused a maximum loss of 2.9% at $\bar{h}_s = 0.714$. However, it may be noted from the Fig. 14(a) and (b) that the percentage of total pressure loss for the zero-strut height itself was about 1% (due to boundary layer and mild shocks in diverging section of the CD nozzle). This shows that the total pressure loss was only about 2% on the account of the strut at its maximum $\bar{h}_s$ under NPR = 3.94. The strut located at $x_s = 0.8L_d$ produced the

https://doi.org/10.1017/aer.2024.121 Published online by Cambridge University Press

next maximum loss of total pressure of about 2.5% at maximum $\bar{h}_s$ at NPR=3.94. From Fig. 14(a) and (b) it can also be observed that for $\bar{h}_s < 0.3$, the strut location relatively had small effect on total pressure loss $\left(p'_{ol}\right)$. In other words, p'_{ol} was not sensitive to x_s for smaller strut heights, i.e. $\bar{h}_s < 0.3$. This was more evident at under-expanding conditions (NPR = 7.89) when compared to over-expanding (NPR = 3.94) conditions. However, as $\bar{h}_s$ was increased, the strut location became important in shaping the total pressure losses. It can also be discerned from Fig. 14(a) and 14(b) that the p'_{ol} Vs $\bar{h}_s$ plots at over-expansion conditions for the strut locations far away from the nozzle throat (x_s=*0.667* L_d and *0.8* L_d), were closer to linearity when compared to those locations that were nearer to the throat, i.e. x_s=*0.33* L_d and *0.5* L_d. It can be noticed from Fig. 14(a) that at larger $\bar{h}_s$, the strut location $x_s = 0.5\ L_d$ caused minimum loss for over-expansion conditions. However, for a given x_s, increase in $\bar{h}_s$ caused an increase in p'_{ol}. This could be due to the fact that as $\bar{h}_s$ increases, the separation shock and the bow shock become less oblique and grow stronger causing larger p'_{ol}. This was, in general, true for all strut locations. However, at over-expansion conditions the behavioural variation of p'_{ol} with $\bar{h}_s$ was unique to a strut location. At under-expansion conditions (Fig. 14(b)), the trend of p'_{ol} vs $\bar{h}_s$ curves was such that for a given $\bar{h}_s$, as x_s was increased, the total pressure loss also increased. This was due to the fact that the strut faced a larger free-stream Mach number as the strut was moved downstream from the throat section, which resulted in a stronger shock wave in front of the strut. This gave rise to larger p'_{ol}. Further, with the interaction of the stronger shock wave, the boundary layer separation on the *SSW* became more significant with more flow separation losses adding to the shock losses, both in the form of total pressure losses. Also, as can be seen from Fig. 14(b), at under-expansion conditions, the location of the strut had little influence on the total pressure loss at smaller values of $\bar{h}_s$, but had noticeable effect at larger $\bar{h}_s$. The variations of total pressure loss with $\bar{h}_s$ at NPR = 7.89 can be reckoned to be closer to linear. Larger pressure losses resulted at larger $\bar{h}_s$ and x_s.

The variation of percentage of thrust loss with strut height are presented in Fig. 15(a) for NPR = 3.94 and in Fig. 15(b) for NPR = 7.89. It can be seen from the figures that the percentage of thrust loss at NPR =3.94 was higher when compared to that at NPR = 7.89 for the same $\bar{h}_s$ and x_s. At NPR = 3.94, the maximum thrust loss was about 3.12% for $\bar{h}_s = 0.714$ and x_s=*0.8* L_d, whereas it was about 2.32% at NPR = 7.89 for the same operational conditions. From Fig. 15(a) and 15(b) it can be observed that in general, as $\bar{h}_s$ was increased the thrust loss also increased at all strut locations. At over-expansion conditions (NPR = 3.94), as x_s was increased, T'_l also increased for a given $\bar{h}_s$ (with the exception of $x_s = 0.8\ L_d$ between $\bar{h}_s = 0.286$ and 0.429) when $\bar{h}_s > 0.143$. The same can be noticed at under-expansion conditions also (Fig. 15(b)). As the internal flow through the nozzle incurs larger total pressure loss at larger $\bar{h}_s$, thrust loss $\left(T'_l\right)$ also increases with increase in p'_{ol}. It is well known that total pressure losses in the internal flow through a propulsion system translate into thrust losses as the thrust produced by a propulsion system is linked to magnitude of the total pressure of the internal flow. Further, it can also be discerned from the figures that as the strut distance from throat section (x_s) was increased, the overall slope of the T'_l vs $\bar{h}_s$ curve did exhibit an increasing trend. This also indicated that as the strut was moved from x_s =0.33 L_d to 0.67 L_d, the sensitivity of T'_l to $\bar{h}_s$ also increased.

4.5 Thrust deflection angle variation with dimensionless strut height

The imbalance of forces perpendicular to nozzle axis due to asymmetric p_w distributions in upper and lower halves of the C–D nozzle manifests as side force either acting upward or downward. The magnitude and direction of side force depends on strut location, strut height and nozzle operating conditions and this was discussed in Section 4.3. This side force shows up as the deflection of thrust vector at the nozzle exit. The variation of thrust deflection angle (δ) with strut height for different strut locations is shown in Fig. 16(a) for NPR = 3.94 and in Fig. 16(b) for NPR = 7.89. The variation of δ with $\bar{h}_s$ for a given strut location is similar to that of side force coefficient variation with $\bar{h}_s$ as depicted in Fig. 13. Ignoring the minor losses in thrust as a result of increase in strut height, the side force F_y is proportional to tan δ. For small δ, tan δ is approximately equal to δ. Hence for small δ, the side force coefficient is proportional to δ. This was brought out in the Fig. 16(a) for NPR = 3.94 and in Fig. 16(b) for NPR = 7.89. It can be

https://doi.org/10.1017/aer.2024.121 Published online by Cambridge University Press

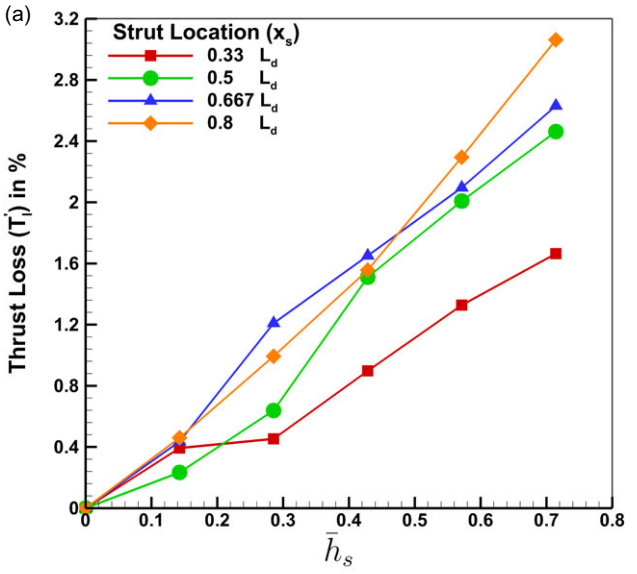

NPR=3.94, over-expansion.

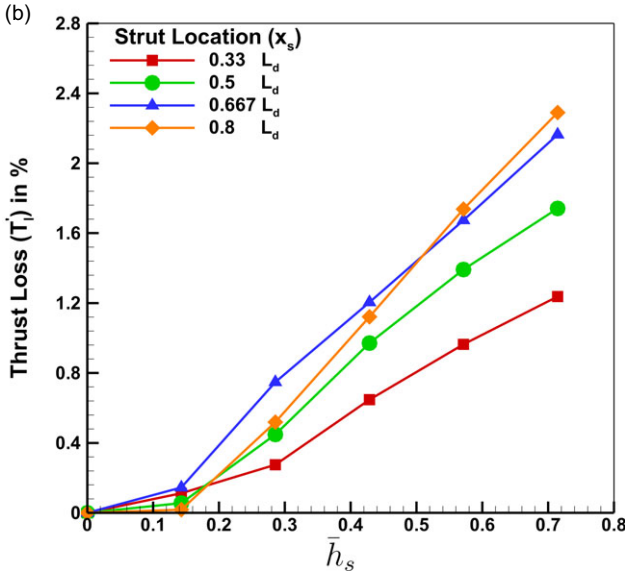

NPR=7.89, under-expansion.

Figure 15. *Variation of thrust loss with strut height, strut location and NPRs.*

seen from Figure 16 that the direction of thrust deflection depends on the position of strut in diverging section of the nozzle. From Fig. 16(a), it can be observed that for strut positions x_s =*0.5* L_d and 0.8 L_d, the sign of δ did not change with respect to $\bar{h}_s$, but for the positions $x_s = 0.33$ L_d and 0.667 L_d the sign depended on $\bar{h}_s$. It can be observed that at $\bar{h}_s = 0.571$, the strut positions $x_s = 0.33$ L_d and 0.667 L_d produced almost negligible thrust deflection at over-expansion conditions. Maximum δ of 4.3° (negative) and 3.90° (positive) were produced by $\bar{h}_s = 0.571$ at $x_s = 0.8L_d$ and $\bar{h}_s = 0.429$ at x_s=$0.5L_d$, respectively. On the other hand, at under-expansion conditions (NPR=7.89), the strut positions at $x_s = 0.5L_d$ and x_s =$0.667L_d$ always produced positive δ at all values of $\bar{h}_s$. The deflection angle δ reached a maximum of 3.2° at $\bar{h}_s = 0.429$ and declined thereafter with increase in $\bar{h}_s$ in case of $x_s = 0.5L_d$. However, when

https://doi.org/10.1017/aer.2024.121 Published online by Cambridge University Press

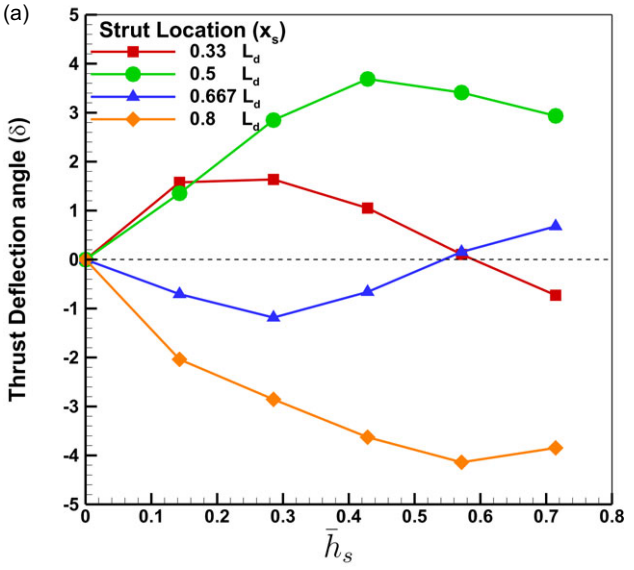

NPR=3.94, over-expansion.

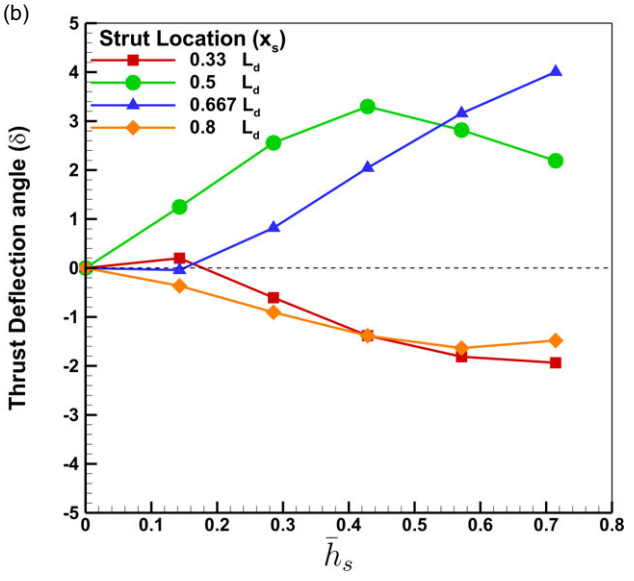

NPR 7.89, under-expansion.

Figure 16. *Variation of thrust deflection angle with strut height, strut location and NPRs.*

$x_s = 0.667L_d$, δ continuously increased and reached a maximum of 4.0° at $\bar{h}_s = 0.714$. The other two extreme positions of strut, i.e. $x_s = 0.337L_d$ and $0.8L_d$ resulted in negative deflections for all values of $\bar{h}_s$.

4.6 Variation of vectoring performance index (VPI) with dimensionless strut height

The variations of VPI with $\bar{h}_s$ for different strut locations are presented in Fig. 17(a) for over-expansion and in Fig. 17(b) for under-expansion conditions. It can be observed that at over-expansion conditions,

https://doi.org/10.1017/aer.2024.121 Published online by Cambridge University Press

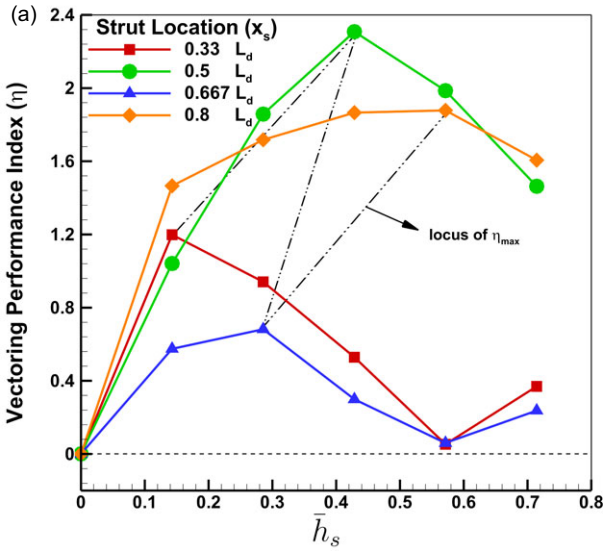

NPR=3.94, over-expansion.

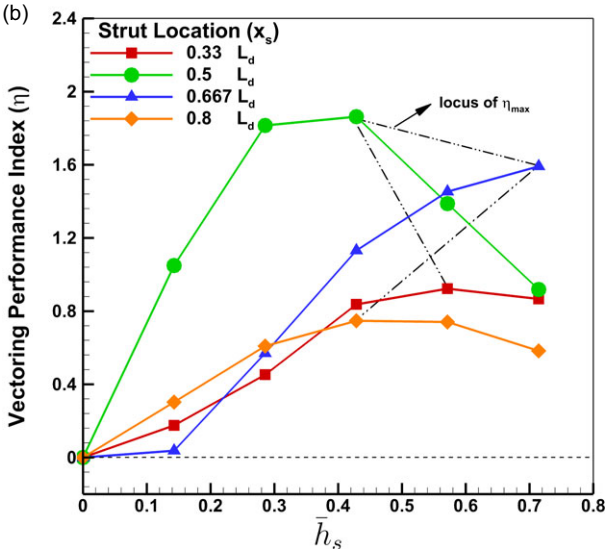

NPR=7.89, under-expansion.

Figure 17. *Variation of Vectoring Performance Index (VPI) with strut height, strut location and NPRs.*

the strut locations *0.5* L_d and *0.8* L_d performed better when compared to other locations. But at under-expansion conditions, the locations *0.5* L_d and *0.667* L_d did show good performance. Hence, at both under and over-expansion conditions, $x_s = 0.5\ L_d$ performed better. However, when larger values of δ are needed at under-expansion, x_s=*0.667* L_d choice is preferred. But for this a large strut height is needed. It is evident that with multiple strut locations such as $x_s = 0.5\ L_d$ and $0.667\ L_d$ on either side of nozzle axis, the full range of thrust deflection angle requirements can be met.

4.7 Deflection of exhaust jet

The path followed by deflected jet at over-expansion (NPR = 3.94) and under-expansion (NPR = 7.89) was determined for various strut heights at two positions $x_s = 0.33\ L_d$ and *0.8* L_d, and this is presented

https://doi.org/10.1017/aer.2024.121 Published online by Cambridge University Press

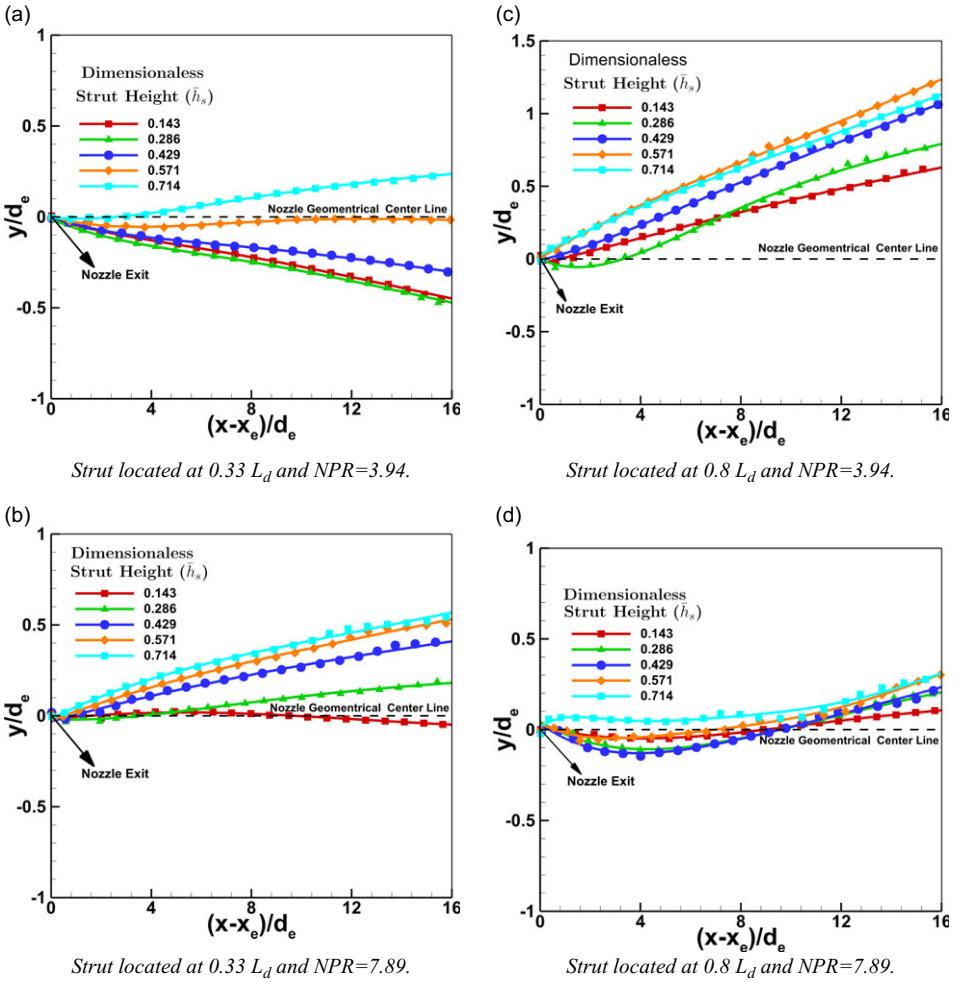

Strut located at 0.33 L_d and NPR=3.94. *Strut located at 0.8 L_d and NPR=3.94.*

Strut located at 0.33 L_d and NPR=7.89. *Strut located at 0.8 L_d and NPR=7.89.*

Figure 18. *Exhaust jet deflection path for strut located at 0.33 L_d and 0.8 L_d at over-expansion and under-expansion conditions.*

in Fig. 18. X-axis represents dimensionless axial distance with origin located at nozzle exit (x_e). Y-axis represents the lateral distance in nominal plane. The trace of jet midline is the locus of midpoint between upper and lower jet boundaries. The jet boundary was defined as locus of points where the flow velocity is 5% of local maximum velocity at $(x\text{-}x_e)/d_e$ in the nominal plane.

It can be observed from Fig. 18(a) that when the strut is located closer to nozzle throat and the nozzle is in over-expansion mode, the jet-axis lies below the nozzle centreline. However, when the strut height is increased, the jet-axis moves closer to the nozzle axis. It is only at very large strut height like $\bar{h}_s = 0.714$, the jet axis is above the nozzle axis and the jet deflection is upwards. However, when the nozzle is operated in under-expansion mode (Fig. 18(b)), even at the small strut heights, the jet-axis is closer to nozzle axis. When the strut height is raised, the upward deflection of the jet axis increases and the jet-axis is always above the nozzle axis. When the strut position is pushed towards the nozzle exit, for example $x_s = 0.8\ L_d$, the over-expansion, however, keeps the jet axis always above the nozzle axis (Fig. 18(c)) and the jet always deflects upwards. For the same strut position, the under-expansion condition (Fig. 18(d)) makes the jet axis hover around the nozzle axis up to $10d_e$ from the nozzle exit. Depending on position of strut insertion, the path of the jet plume varies.

https://doi.org/10.1017/aer.2024.121 Published online by Cambridge University Press

5.0 Conclusions

The cold flow analysis of the strut insertion-based TVC system indicates that it can be used as a potential alternative TVC system for SITVC system for space launch vehicles. Its use can be made where weight and space requirements are a big constraint for upper stage propulsion modules and where thrust vectoring is needed frequently and for a large operational time. From the present study, the following conclusions can be made.

1. Thrust deflection angles between $+4°$ and $-4°$ can be achieved by inserting a circular rod through nozzle wall in the diverging section of a supersonic nozzle using different combinations of $\bar{h_s}$ and x_s. The maximum vectoring performance index 'η' that could be attained was 2.32 at over-expansion conditions and 1.82 at under-expansion conditions when $x_s = 0.5L_d$ and $\bar{h_s} = 0.429$, at both the expansion conditions.
2. For a fixed area-ratio nozzle, at low altitudes (over-expansion conditions) it was observed that the thrust vector deflection whether upward or downward depends more on the strut location rather than on strut height. For locations closer to nozzle throat the thrust vector deflection tends to be downward with upward vehicle side force ($x_s \leq 0.5L_d$). In case of locations far away from nozzle throat ($x_s = 0.8L_d$) the opposite, i.e. upward thrust vector deflection with downward vehicle side force occurs for all strut heights. Large thrust vector deflection angles could be achieved at $0.5L_d$ and $0.8L_d$ strut locations by varying strut height. Negative thrust vector deflection (downward deflection) occurred for all strut heights at $0.5\ L_d$ whereas $0.8\ L_d$ location produced positive deflection (upward deflection) at all strut heights. Maximum deflection in both cases was about $4°$.
3. At high altitudes (under-expansion conditions), variation of strut height at strut locations closer to nozzle throat ($x_s = 0.33L_d$) and far away ($x_s = 0.8L_d$) from it produced upward deflection of thrust vector (with downward vehicle side force), whereas at intermediate locations ($x_s = 0.5L_d$ *and* $0.667L_d$) caused downward deflection (with upward vehicle side force). The vectoring performance with change in $\bar{h_s}$ was better with $x_s = 0.5L_d$ and $x_s = 0.667L_d$ cases.

Acknowledgements. The authors would like to acknowledge the department of aerospace engineering, MIT campus, Anna University, Chromepet for providing computational facility and license for ANSYS CFD Solver to carry out present numerical study.

The authors would like to acknowledge the Council of Scientific and Industrial Research (CSIR), New Delhi, India, vide Sanction ACK no.09/468(540)/2019-EMR-I for providing financial support to the first author by way of granting fellowship during his Research work. The authors are thankful to the colleagues in the laboratory for their help during this study.

Competing interests. The authors declare that they have no known competing financial interests or personal relationships that could have appeared to influence the work reported in this paper.

References

[1] Wu, K., Zhang, G., Kim, T.H. and Kim, H.D. Numerical parametric study on three-dimensional rectangular counter-flow thrust vectoring control, *Proc. Inst. Mech. Eng. G. J. Aerosp. Eng.*, 2020, **234**, pp 2221–2247. https://doi.org/10.1177/0954410020925602

[2] Sung, H.G. and Heo, J.Y. Fluidic thrust vector control of supersonic jet using coflow injection, *J. Propuls. Power*, 2012, **28**, (4), pp 858–861. https://doi.org/10.2514/1.B34266

[3] Zmijanovic, V., Lago, V., Sellam, M. and Chpoun, A. Thrust shock vector control of an axisymmetric conical supersonic nozzle via secondary transverse gas injection, *Shock Waves*, 2014, **24**, (1), pp 97–111. https://doi.org/10.1007/s00193-013-0479-y

[4] Forghany, F., Taeibe-Rahni, M., Asadollahi-Ghohieh, A. and Banazdeh, A. Numerical investigation of injection angle effects on shock vector control performance, *Proc. Inst. Mech. Eng. G. J. Aerosp. Eng.*, 2019, **233**, (2), pp 405–417. https://doi.org/10.1177/0954410017733292

[5] Wu, K. and Dong Kim, H. Numerical study on the shock vector control in a rectangular supersonic nozzle, *Proc. Inst. Mech. Eng. G. J. Aerosp. Eng.*, 2019, **233**, (13), pp 4943–4965. https://doi.org/10.1177/0954410019834133

[6] Das, A.K., Acharyya, K., Mankodi, T.K. and Saha, U.K. Fluidic thrust vector control of aerospace vehicles: State-of-the-art review and future prospects, *J. Fluids Eng.*, 2023, **145**, (8), https://doi.org/10.1115/1.4062109

https://doi.org/10.1017/aer.2024.121 Published online by Cambridge University Press

[7] Hollstein, H.J. Jet tab thrust vector control, *J. Spacecr Rockets*, 1965, **2**, (6), pp 927–930. https://doi.org/10.2514/3.28316

[8] Cong, R., Ye, Y., Zhao, Z., Wu, J. and Zhang, C. Numerical research on jet tab thrust vector nozzle aerodynamic characteristics, *J. Phys. Conf. Ser.*, 2019, **1300**, (1), p 012089. https://doi.org/10.1088/1742-6596/1300/1/012089

[9] Kong, F., Jin, Y., and Kim, H.D. Thrust vector control of supersonic nozzle flow using a moving plate, *J. Mech. Sci. Technol.*, 2016, **30**, (3), pp 1209–1216. https://doi.org/10.1007/s12206-016-0224-4

[10] Kostic, O., Stefanovic, Z., and Kostić, I. Comparative CFD analysis of a 2D supersonic nozzle flow with jet tab and jet vane, *Tehnicki vjesnik – Tech. Gazette*, 2017, **24**, (5). https://doi.org/10.17559/TV-20160208145336

[11] Tammabathula, V.S.M., Ghanta, V.S.K. and Bandla, T.N.S. Effect of flat wall length on decay and shock structure of a supersonic square wall jet, *Proc Inst Mech Eng G J Aerosp Eng*, 2022, **236**, (11), pp 2271–2280. https://doi.org/10.1177/09544100211058016

[12] Samar, R., Zahir, S., and Khan, M.A. Flight control using pin-protuberances for blunted cones, Aeronaut. J., 2010, 114, (1154), pp 245–257. https://doi.org/10.1017/S0001924000003699

[13] Massey, K., Guthrie, K. and Silton, S. Optimized guidance of a supersonic projectile using pin based actuators, In *23rd AIAA Applied Aerodynamics Conference*. American Institute of Aeronautics and Astronautics, 2005, https://doi.org/10.2514/6.2005-4966

[14] Sedney, R. A survey of the effects of small protuberances on boundary-layer flows, AIAA J., 1973, 11, (6), pp 782–792. https://doi.org/10.2514/3.50520

[15] Gang, D., Yi, S. and He, L. Characteristics of the cylinder-induced shock wave and turbulent boundary layer interactions, *J. Vis. (Tokyo)*, 2016, **19**, (4), pp 581–585. https://doi.org/10.1007/s12650-016-0354-x

[16] Ozcan, O. and Yuceil, B.K. Cylinder-induced shock-wave boundary-layer interaction, *AIAA J*, 1992, **30**, (4), pp 1130–1132. https://doi.org/10.2514/3.11039

[17] Stephen, E.J., O'Connell, S., Bertrand, W. and McLaughlin, T.E. Effects of the presence of control fins on the flow around cylindrical protuberances in supersonic crossflow. In *2018 AIAA Aerospace Sciences Meeting*. American Institute of Aeronautics and Astronautics, 2018. https://doi.org/10.2514/6.2018-1514

[18] P.S., V.R., Das, S. and Kim, H.D. Influence of vortex generator on cylindrical protrusion aerodynamics at various Mach Numbers, Aerosp. Sci. Technol., 2016, 58, pp 267–274. https://doi.org/10.1016/j.ast.2016.08.025

[19] Cavalleri, R., Tiarn, W. and Readey, H. Thrust vector control using movable probes, In *28th Aerospace Sciences Meeting*. American Institute of Aeronautics and Astronautics, 1990. https://doi.org/10.2514/6.1990-562

[20] Tiarn, W., and Cavalleri, R., CFD Evaluation of an Advanced Thrust Vector Control Concept, In: 26th Joint Propulsion Conference. American Institute of Aeronautics and Astronautics; 1990. https://doi.org/10.2514/6.1990-1900

[21] Ben Rose, D.B. and Sridhar, B. An experimental investigation on the use of a rectangular strut in a scramjet thruster for thrust vector control, Proc. Inst. Mech. Eng. G. J. Aerosp. Eng., 2021, 235, (11), pp 1374–1384. https://doi.org/10.1177/0954410020973128

[22] Ben Rose, D.R.B. and Sridhar, B.T.N. A rectangular strut on the expansion ramp of a scramjet thruster for thrust vector control, *Acta Astronaut.*, 2022, **194**, pp 9–21. https://doi.org/10.1016/j.actaastro.2022.01.041

[23] Srinivas, A.L. and Sridhar, B.T.N. Experimental study of the wall pressure distribution in a convergent-divergent nozzle with strut injection, *Fluid Dynam.*, 2020, **55**, (2), pp 279–290. https://doi.org/10.1134/S0015462820010139

[24] Lakshmi Srinivas, A., and Sridhar, B.T.N. Experimental study of internal forces and moments generated by strut injection in a supersonic cross-flow in a C-D nozzle, *J. Braz. Soc. Mech. Sci. Eng.*, 2021, **43**, (2), p 84. https://doi.org/10.1007/s40430-020-02771-y

[25] Wu, K. Study on aerodynamic features of rod thrust vector control for physical applications, *Proc. Inst. Mech. Eng. G. J. Aerosp. Eng.*, 2021, **237**, (1), pp 156–176. https://doi.org/10.1177/09544100221095363

[26] Soundararajan, H., and B.T.N., S. Numerical study on strut insertion based thrust vectoring control system, *Aircr. Eng. Aerosp. Technol.*, 2023, **95**, (2), pp 201–213. https://doi.org/10.1108/AEAT-12-2021-0387

[27] Srinivas, A.L. and Sridhar, B.T.N. Experimental study of strut insertion technique in a convergent-divergent nozzle for thrust vector control, *Instrum. Exp. Techniq.*, 2022, **65**, (1), pp 132–141. https://doi.org/10.1134/S0020441222010122

[28] Model 9116 Intelligent Pressure Scanner User's Manual, 2007.

[29] ANSYS CFX-Solver Theory Guide, 2009.

[30] ICEM CFD User Manual, 2011.

[31] Tulapurkara, E.G. Turbulence models for the computation of flow past airplanes, *Progr. Aerosp. Sci.*, 1997, **33**, (1–2), pp 71–165. https://doi.org/10.1016/S0376-0421(96)00002-4

[32] Hadjadj, A., Perrot, Y. and Verma, S. Numerical study of shock/boundary layer interaction in supersonic overexpanded nozzles, *Aerosp. Sci. Technol.*, 2015, **42**, pp 158–168. https://doi.org/10.1016/j.ast.2015.01.010

[33] Roache, P.J. Perspective: A method for uniform reporting of grid refinement studies, *J. Fluids Eng.*, 1994, **116**, (3), pp 405–413. https://doi.org/10.1115/1.2910291

Cite this article: Soundararajan H. and Sridhar B.T.N. Study of performance of an internal strut-based thrust vectoring control system. *The Aeronautical Journal*, https://doi.org/10.1017/aer.2024.121